Nanotechnology

PAPER

Functionalized magnetic composite nano/microfibres with highly oriented van der Waals CrI_3 inclusions by electrospinning

To cite this article: Vahideh Bayzi Isfahani *et al* 2021 *Nanotechnology* **32** 145703

View the article online for updates and enhancements.

IOP ebooks™

Bringing together innovative digital publishing with leading authors from the global scientific community.

Start exploring the collection–download the first chapter of every title for free.

This content was downloaded from IP address 193.137.92.159 on 12/01/2021 at 09:59

IOP Publishing Nanotechnology
Nanotechnology 32 (2021) 145703 (12pp) https://doi.org/10.1088/1361-6528/abd4a3

Functionalized magnetic composite nano/microfibres with highly oriented van der Waals CrI_3 inclusions by electrospinning

Vahideh Bayzi Isfahani[1,*], João Filipe Horta Belo da Silva[2], Loukya Boddapati[3], Anabela Gomes Rolo[1], Rosa Maria Ferreira Baptista[1], Francis Leonard Deepak[3], João Pedro Esteves de Araújo[2], Etelvina de Matos Gomes[1] and Bernardo Gonçalves Almeida[1,*]

[1] Centro de Física das Universidades do Minho e Porto, Departamento de Física, Universidade do Minho, Campus de Gualtar, 4710-057, Braga, Portugal
[2] IFIMUP—Instituto de Física de Materiais avançados, Nanotecnologia e Fotónica, Universidade do Porto, DFA-FCUP, R. Campo Alegre, 4169-007 Porto, Portugal
[3] Nanostructured Materials Group, International Iberian Nanotechnology Laboratory(INL), Avenida Mestre Jose Veiga, Braga 4715-330, Portugal

E-mail: v.b.isfahani@gmai.com and bernardo@fisica.uminho.pt

Received 25 September 2020, revised 11 December 2020
Accepted for publication 17 December 2020
Published 11 January 2021

Abstract

This study reports on the synthesis of highly oriented chromium triiodide (CrI_3) magnetic inclusions inside nano/microfibres with a polyethylene oxide matrix, prepared by the electrospinning technique. The structural, microstructural and spectroscopic analysis shows uniformly dispersed CrI_3 nanosized inclusions inside the fibres, presenting a C2/m monoclinic structure at room temperature, where their *c*-axis is perpendicular to the fibre mat plane and the ab layers are in-plane. Analysis of the magnetic properties show that the samples have a ferromagnetic–paramagnetic phase transition at ∼55–56 K, lower than that of bulk CrI_3. Noticeably, a field-driven metamagnetic transition is observed below ∼45 K, from *M* versus *H* curves, when the applied magnetic field is perpendicular to the fibre mat plane, while it is strongly reduced when the field is in-plane. This anisotropic behaviour is attributed to the field-induced changes from antiferromagnetic to ferromagnetic interlayer magnetic moment alignment along the CrI_3 *c*-axis stacked layers. These CrI_3 electrospun fibres then show an efficient cost-effective route to synthesize magnetic composite fibres with highly oriented van der Walls inclusions, for spintronic applications, taking advantage of their anisotropic 2D layered materials properties.

Supplementary material for this article is available online

Keywords: nano/microfibres, electrospinning, 2D magnets, magnetic properties, spintronic, CrI3, functional systems

(Some figures may appear in colour only in the online journal)

1. Introduction

Since the discovery of graphene in 2004 [1], two-dimensional (2D) materials have attracted a great deal of research interest. The exceptional properties of graphene have motivated researchers to explore graphene-like 2D compounds and explore new applications. Due to this, a wide array of optical, mechanical, chemical and electrical phenomena has been realized in 2D crystals [2–7]. On the other hand, ferromagnetic (FM) materials are promising candidates for several

* Authors to whom any correspondence should be addressed.

 © 2021 IOP Publishing Ltd Printed in the UK

interesting applications such as spintronic devices [8, 9], data storage [10], sensing [11, 12], magnetoelectronic technologies [13–15] or in biomedical application [16, 17] such as magnetic labelling and hyperthermia treatment of tumours. In this respect, materials composed by 2D layers bonded to one another through weak van der Waals interactions present enormous potential for several of these applications and, in particular, for spintronics [18]. They often exhibit strongly anisotropic behaviour and can be cleaved into very thin specimens, frequently monolayer crystals [19]. In this regard, chromium trihalides, CrX_3 (X = Cl, Br, I), chromium dihalides [19, 20], and chromium-based ternary compounds such as $CrXTe_3$ (X = Si, Ge) and $Cr_2X_2Te_6$ (X = Si, Ge, Sn), are excellent examples of layered *FM* semiconductors with weak interlayer van der Waals interactions [19].

Recently, reports have been focusing on evaluating different properties of CrI_3 layers prepared by chemical vapour transport (CVT) [21, 22]. CrI_3 has intrinsic ferromagnetic nature and one of the highest Curie temperatures (T_c) of the trihalides, at about 61 K in its bulk form [22, 23]. In CrI_3, the number of the layers [24] and stacking arrangement [25, 26] directly affects their magnetic properties. While CrI_3 monolayers are ferromagnetic [20] with the $T_c \sim 45$ K, antiferromagnetism has been observed in CrI_3 bilayers [19, 27, 28] whereas trilayers are, again, ferromagnetic [7]. These properties arise from the competition between two interactions; first the direct exchange between Cr–Cr which is antiferromagnetic (AFM) in nature and second, the superexchange interaction mediated through iodine nonmagnetic ligand ion. The superexchange interaction can lead to FM if the Cr–I–Cr angle is 90º, while it results in AFM when the angle is 180º [23, 29]. This was referred to recently as the origin of the increasing Curie temperature and decreasing magnetization of 2D CrI_3 under hydrostatic pressure, where the applied pressure can affect both the coupling between the layers as well as Cr–I–Cr angle [23]. Controlling the CrI_3 crystals thickness is another approach for engineering the magnetic critical properties, especially magnetic transitions, proposed by Yu Liu *et al* [22]. In particular, the reduction of thickness can induce the presence of a metamagnetic transition in the sample, under the application of an out of plane external magnetic field [22]. Electrical modulation of the CrI_3 magnetic state is another property of CrI_3, which makes it particularly interesting for applications in spintronic devices. Recently, it has been shown that the electric field can induce the interlayer antiferromagnetic-to-ferromagnetic phase transition in CrI_3 bilayers, with a relatively low critical field [30].

An overview of previous research on CrI_3 shows that although this material has been of great interest to researchers in recent years, its synthesis by alternative methods has not been considered. In other words, in most of the reported research, a bulk sample has been prepared by the CVT method and CrI_3 monolayer, bilayer or multi-layer samples are then, typically, made by mechanical exfoliation methods [20, 28]. This is a cumbersome sample preparation procedure and the resultant samples are prone to light, air and moisture induced degradation [31]. To prevent the latter, new and efficient synthetic strategies and storage methods are required [31, 32].

To design efficiently aligned 2D magnetic material devices, it is very important to control their morphology and magnetization orientation, to take advantage of the CrI_3 anisotropic magnetic properties. In this regard, the electrospinning technique is a relatively simple and low-cost technique, which has been significantly developed in recent years [33, 34]. Current applications of electrospun magnetic nano/microfibres include data storage and transfer devices [35], microwave absorption and electromagnetic shielding [36], biomedical [37], drug delivery [38] or magnetic sensors [34]. In particular, electrospinning is a very powerful tool for controlling the morphology and molecular orientation of the polymer chains along electrospun fibers with different polymers and inclusions [39–41]. Electrospinning is based on the extrusion of a thin fibre from an electrically charged polymer solution provoked by a strong applied DC electric field [39]. A viscous precursor solution is formed when the polymer is mixed with the active functionalizing inclusions. The solution is then loaded into a syringe with its needle connected to a high voltage source. At the threshold voltage, when the electrostatic forces overcome the surface tension of the precursor solution, the polymer droplet at the end of the needle is shaped into a Taylor cone and is continuously drawn into a fibre jet. The fibres are, in general, collected as a mesh on a grounded collector plate. The electrospun fibre diameters can vary from several nanometers up to several micrometres, depending on the parameters of the process, while their lengths can reach several meters. The polymer chain orientation along the electrospun fibre is caused by shear stress and Coulombic forces acting on the polymer solution as the jet is accelerated by the electric field. This electrostatic alignment originated by the electrospinning process should be effective for creating oriented inclusions inside the polymer matrix, which suggests that the electrospinning technique can be used for producing fibre arrays with anisotropic properties.

In this article, we demonstrate the implementation of this approach for the production of oriented CrI_3 inclusions with anisotropic magnetic properties, inside nano/microfibre arrays of polyethylene oxide (PEO) fibres, by the electrospinning technique. Therefore, the present study has focused on the fabrication and characterization of magnetic fibre mats consisting of PEO polymer and CrI_3 nanopowder, aiming at magnetically oriented encapsulation of CrI_3 inside the polymer fibres. The samples are identified as PC_x in which x represents the mass amount of CrI_3 as the precursor. Reliance on the electrospinning method as a cost-effective and affordable method to take advantage of the anisotropic magnetic properties of these 2D materials, as well as the use of PEO as a non-toxic suitable carrier for electrospinning, are the key advantages of the proposed method.

2. Experimental

Polyethylene oxide (PEO) polymer, with an average molecular weight 300 000, and 2-Propanol (99.7%), as the solvent,

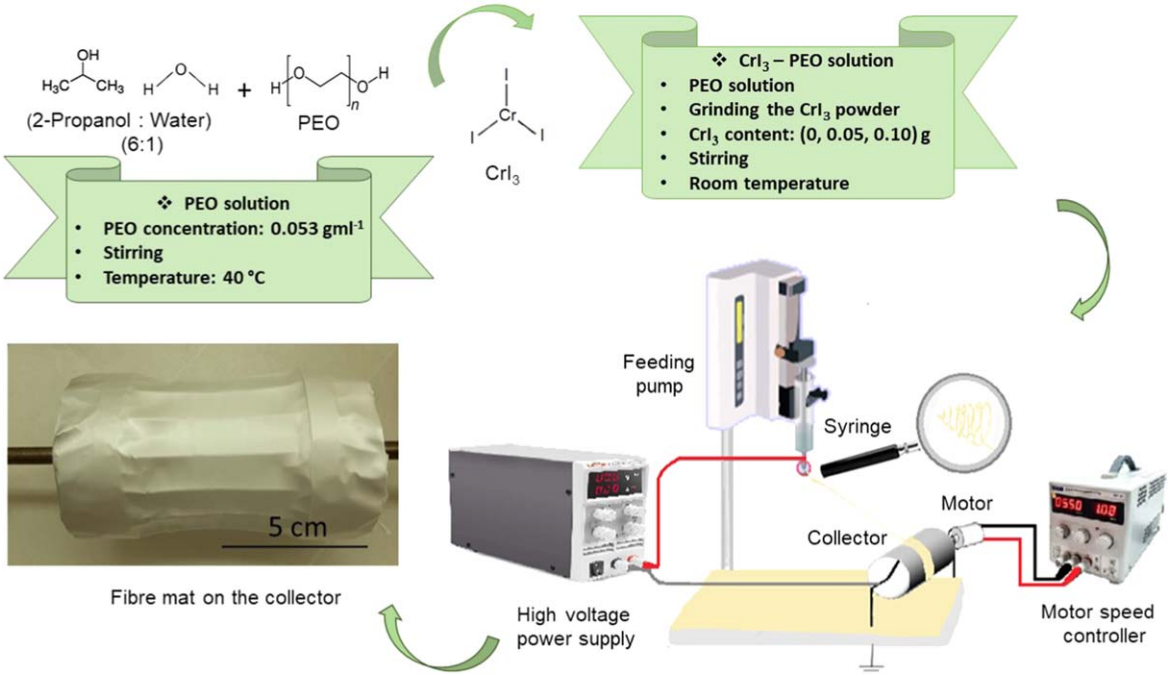

Figure 1. Samples preparation scheme and physical appearance of the PC_x mat.

were acquired from Sigma-Aldrich and Merck, respectively. These materials were used without further purification. Distilled water was also used to obtain high purity solutions. Figure 1 summarizes the synthesis procedure of the fibre mats. Using 2-Propanol and water (as solvents with the ratio of 6:1), a solution with a 0.053 gml^{-1} PEO concentration was prepared (PEO solution). These ratios were chosen after several experiments to make the solution suitable for electrospinning and taking into account previous work with this polymer [42, 43].

In the next step, different amounts of chromium (III) iodide powder (99%), which was purchased from Apollo Scientific, were added to the PEO solution and followed by magnetic stirring (CrI_3–PEO solution). The CrI_3 powder was previously grinded in an agate mortar, before use, to obtain smaller particles. The initial particle sizes were several micrometers or larger (supplementary figure S1 (available online at stacks.iop.org/NANO/32/145703/mmedia)). These steps were performed under Ar flux to prevent CrI_3 degradation (hydration). Since PEO is easily soluble in the 2-propanol-water solvent mixture, the used stirring improves its dissolution. On the other hand, CrI_3 is almost insoluble in it. So, the magnetic stirring leads to a homogeneous suspension of CrI_3 particles in the solution. These obtained precursor solutions with different CrI_3 concentrations were then used in the electrospinning method to make the fibre mat samples. They are represented by the PC_x notation where P and C represent PEO and CrI_3, respectively, and x stands for the CrI_3 mass used in the 7 ml base solution. Three different masses (x values) were prepared: 0, 0.05 and 0.10 g.

The nano/microfibres fabrication by electrospinning, using the PC_x solutions, was achieved by applying a DC voltage of 20 kV to the needle (25 G—ISO 9626:2001, with 0.5 mm outer diameter and 0.232 mm inner diameter) that was attached to a 5 ml syringe containing the prepared solution. The grounded collector of the fabricated fibres was an aluminium foil that was placed at a distance of 12 cm from the needle tip. The flow rate was fixed at 0.5 ml h^{-1} using a syringe pump. The electrospinning process was carried out under ambient conditions.

The crystalline structure and phase purity of the samples was studied by x-ray diffraction (XRD) with a Bruker D8 Discover diffractometer using Cu-Kα radiation ($\lambda = 1.540\,60$ Å) at 40 kV and 40 mA and Bragg-Brentano geometry. Each sample was scanned in the 2θ range: 10°–80° at a speed of 0.04 $°s^{-1}$.

The morphology of the electrospun PC_x fibre mats and CrI_3 precursor powder was characterized by an Ultra-high resolution field emission gun scanning electron microscope (FEG-SEM), NOVA 200 Nano SEM, FEI Company. Secondary electron images were obtained at an acceleration voltage between 5 and 10 kV to acquire morphological information. Atomic contrast images were acquired with a Backscattering electron detector at an acceleration voltage of 15 kV.

Microanalysis of the samples to obtain the chemical composition were performed with the energy dispersive spectroscopy technique, using an EDAX Si (Li) detector at an acceleration voltage between 15 and 20 kV. Samples surfaces were covered with a conductive thin film (15 nm) of Au–Pd (80–20 weight %), using a high-resolution sputter coater, 208HR Cressington Company, coupled to a MTM-20 Cressington High Resolution Thickness Controller. The average fibre diameters were estimated from FEG-SEM image analysis, by using ImageJ software, at different areas, for each sample. High magnification imaging of the fibres was performed by scanning transmission electron microscopy (STEM) at 80 kV using high angle annular dark field (HAADF) detector in Probe-corrected FEI Titan G2 ChemiSTEM (80–200 kV).

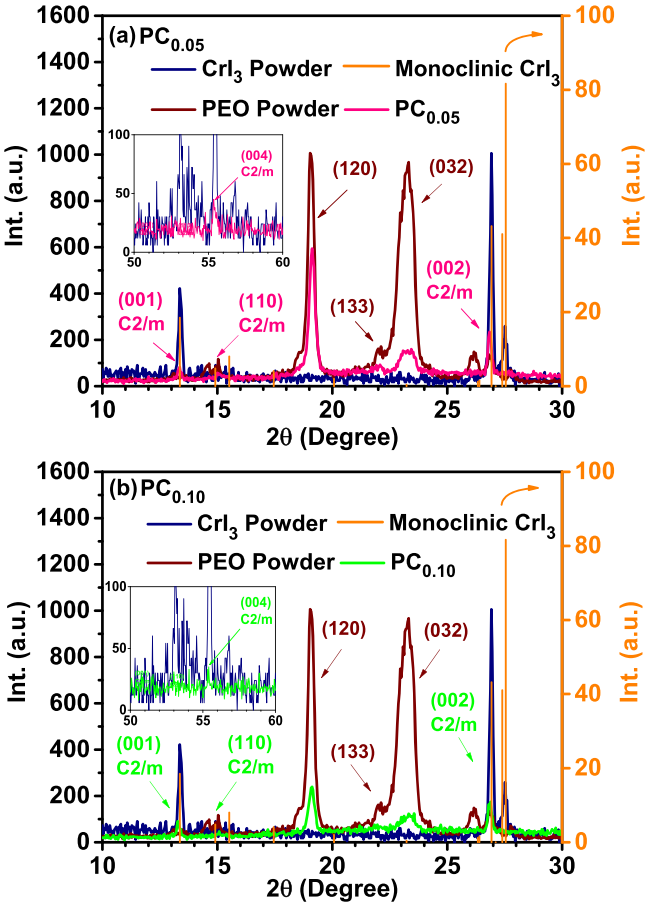

Figure 2. A comparison between XRD patterns of the $PC_{0.05}$ (a) and $PC_{0.10}$ (b) electrospun samples with CrI_3 and PEO powder XRD pattern (left axis), including the CrI_3 reference peaks according to the C2/m monoclinic structure from [20] (right axis). The insets present the (004) small peak corresponding to the CrI_3 $C2/m$ monoclinic structure around 55.50°.

The magnetic properties of the samples were analyzed using a Quantum Design MPMS SQUID magnetometer. Thermomagnetic analysis was performed both under zero-field cooled (ZFC) and field-cooled (FC) procedures. Isothermal magnetization hysteresis cycles were measured at different temperatures, from 5 to 300 K, between −10 kOe and up to +50.2 kOe.

3. Results and discussion

3.1. Structural analysis

Figure 2 presents the XRD patterns of the PC_x samples ($x = 0$, 0.05 and 0.10 g) along with pure PEO and CrI_3 powder, used in the preparation of the fibre mats. At room temperature chromium triiodide presents a $C2/m$ monoclinic phase [20] whose peak positions are marked by vertical lines in figure 2 (corresponding to the right axis of the figure). Here, the close matching between the CrI_3 powder peak positions and the reference marks indicates that the CrI_3 powder used for the sample preparation process has the $C2/m$ monoclinic phase.

By comparing the XRD results of the nano/microfibre samples with the PEO powder pattern, it is possible to observe that the peaks obtained at 19.09° and 23.30° are the most intense characteristic peaks of the crystalline structure of PEO polymer. On the other hand, in the fibres, two other peaks are observed at 13.38° and 26.74° that present increasing relative intensities with increasing amount of added CrI_3. These peaks are in good agreement with the (001) and (002) peaks of the room temperature monoclinic structure of CrI_3. The relative intensity for $I_{CrI_3,(001)}/I_{PEO,(120)}$ and $I_{CrI_3,(002)}/I_{PEO,(120)}$ ratios are, approximately, 11% and 33% in the $PC_{0.05}$ sample, respectively, and increase to 33% and 64% in $PC_{0.10}$, consistent with the increase of CrI_3 inclusions concentration in the fibres. Additional small (110) and (004) peaks are observed, near 15.52° and 55.50°, which also correspond to the CrI_3 $C2/m$ monoclinic structure. This suggests that the chromium iodide inclusions have grown mainly oriented within the nano/microfibres, where their *c*-axis is perpendicular to the fibre mats plane. Considering that the fibres are in-plane, this indicates that the CrI_3 c-axis is perpendicular to the fibre axis and is along the fibre radial direction. Therefore, the hexagonal CrI_3 layer planes are along the nano/microfibre axis. Nevertheless, the presence of the small (110) peak, near 15°, indicates some degree of polycrystallinity in the samples.

At low temperature, in the ferromagnetic phase, CrI_3 changes to an $R\bar{3}$ structure, due to lateral shifts of the *ab* hexagonal layers [26]. Since the CrI_3 layers are essentially identical in both the high- and low-temperature structures the same relative orientation of the CrI_3 inclusions is expected to be maintained in the ferromagnetic phase [20, 26].

Another point worth highlighting is that the relative intensity $I_{PEO,(032),(133)}/I_{PEO,(120)}$ decreases from ∼95% in the PEO powder to ∼12% in the fibre mats. A similar reduction of the relative intensity ratios $I_{PEO,Peaks}/I_{PEO,(120)}$ of the other PEO peaks is observed in the nano/microfibres, as compared to their bulk counterparts. This indicates that PEO also tends to grow oriented with the [120] direction perpendicular to the fibre mats plane, so that the polymer backbones are predominantly along the PEO fibre axes [44], due to the directional shear stresses and charge repulsion developed as the electric field stretches the emitted jet during the electrospinning process [39, 41]. On the other hand, bulk CrI_3 is formed by stacked layers with weak interlayer van der Waals interactions, along the *c*-axis direction [20]. When CrI_3 is grinded, it tends to form plate-like particles with high width-to-thickness aspect-ratio. Initially, in the precursor solution, the CrI_3 particles are randomly oriented. However, due to the developed directional shear forces, coupled with the strong electric field, and the sink-like flow in the electrospinning needle [39, 45], the CrI_3 flakes are gradually oriented mainly along the streamlines, as the jet is emitted. Subsequently, as the jet dries in its path towards the electrode, the CrI_3 particles orientation is kept fixed inside the fibres. This then leads to the formation of electrospun fibre mats with oriented CrI_3 inclusions inside them, as observed in our samples. This effect has been also observed with other rodlike and platelike inclusions in electrospun fibres [45, 46].

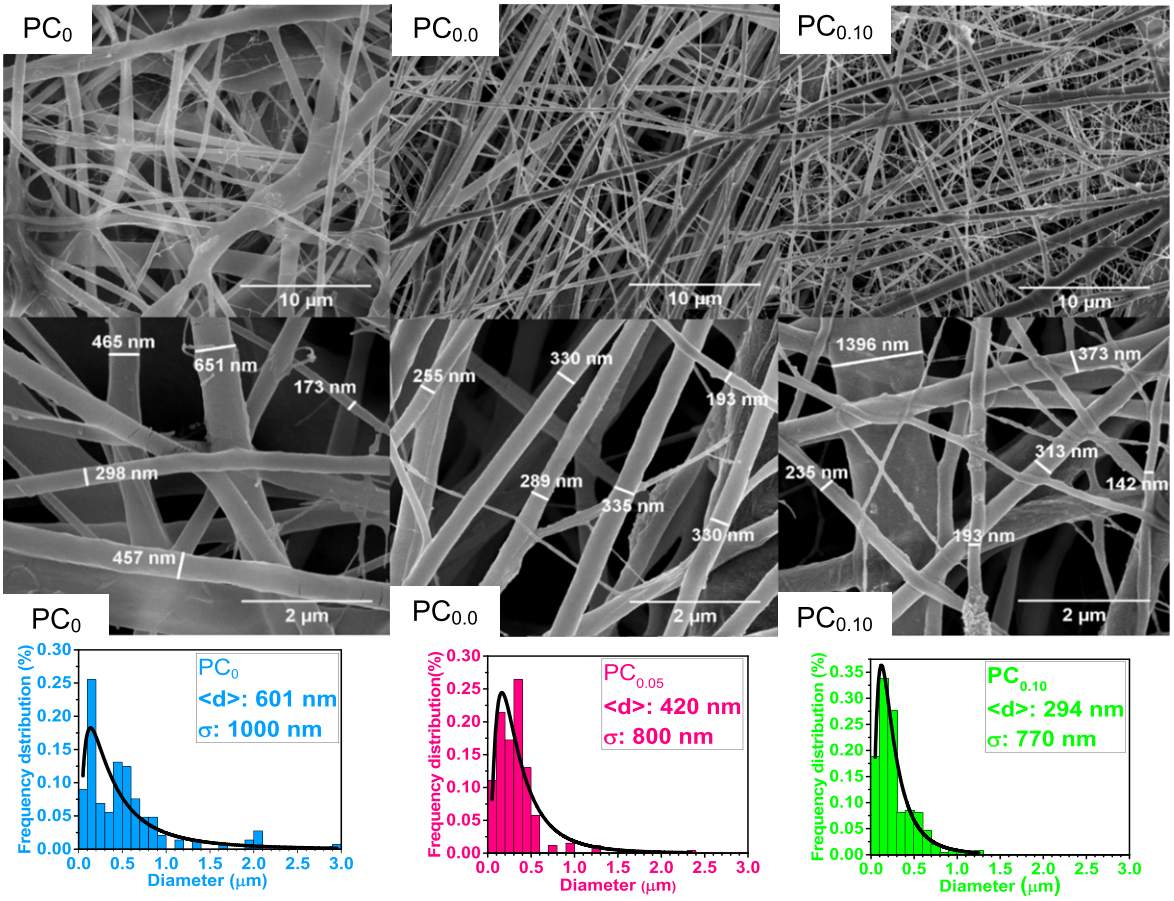

Figure 3. Comparison between SEM images of PC_0 (left), $PC_{0.05}$ (middle) and $PC_{0.10}$ (right) along with their diameter distribution function.

The CrI_3 XRD peaks in the PC_x samples were fitted with Voigt functions to determine their peak positions and widths. The size (D) of the included grains inside the fibres can be estimated using the Scherrer equation (1). In this equation β is the full width at half maximum of the peak, 2θ is the diffraction angle in radians and λ is the wavelength used in this analysis ($\lambda = 1.540\,60$ Å)

$$D = \frac{0.9\lambda}{\beta \cos\theta}. \tag{1}$$

The grain size of the CrI_3 inclusions was evaluated using their (002) peak in the fibre mats (which is more intense and well defined) and their values were approximately 46 nm for $PC_{0.05}$ and 42 nm for the $PC_{0.10}$ sample. Furthermore, the strain (ε) in the CrI_3 inclusions inside the fibre was calculated from the observed shift of the XRD peak position in the fibres, relative to the bulk value, using equation (2):

$$\varepsilon = \frac{d_{\text{exp}} - d_{\text{ref}}}{d_{\text{ref}}}. \tag{2}$$

In this equation, d_{exp} and d_{ref} are the experimental and reference lattice spacing values, respectively. d_{exp} is evaluated from the fitted peak positions and d_{ref} is obtained from the $C2/m$ monoclinic structure of CrI_3 [20]. The evaluated strain, from the (002) peak in the XRD pattern, is about –0.08%, 0.23% and 0.19% for CrI_3 powder, $PC_{0.05}$ and $PC_{0.10}$, respectively. Given that the incident beam in XRD analysis scans the atomic planes direction perpendicular to the PC_x fibre mat surface, this indicates the presence of a biaxial expansion strain in plane of the fibre mats and correspondingly within CrI_3 hexagonal ab planes of the grains.

3.2. Morphological analysis

To perform the morphological investigation of the electrospun PC_x fibre mats, FEG-SEM was used and the corresponding analysis were carried out.

Figure 3 shows the FEG-SEM images of the produced fibres, with two different magnifications. As illustrated in this figure, these fibre mats are made of a network of randomly aligned fibres. To estimate the diameter of the fibres, several of them were measured for each different nano/microfibre sample. The evaluation was carried out over a large area, with a 100 μm^2 average size, to be statistically significant. The results of these measurements are also presented in the form of the frequency bar graphics in this figure. The diameter sizes were modelled using a log-normal distribution that was fitted to the experimental points, as also shown in figure 3.

Both the average diameter $\langle d \rangle$ and their distribution width σ decrease with increasing CrI_3 content. Progressively adding CrI_3 to the PEO polymer matrix promotes the presence of a collection of thin composite fibres, with diameters that are lower and more uniform (lower σ) as the concentration of

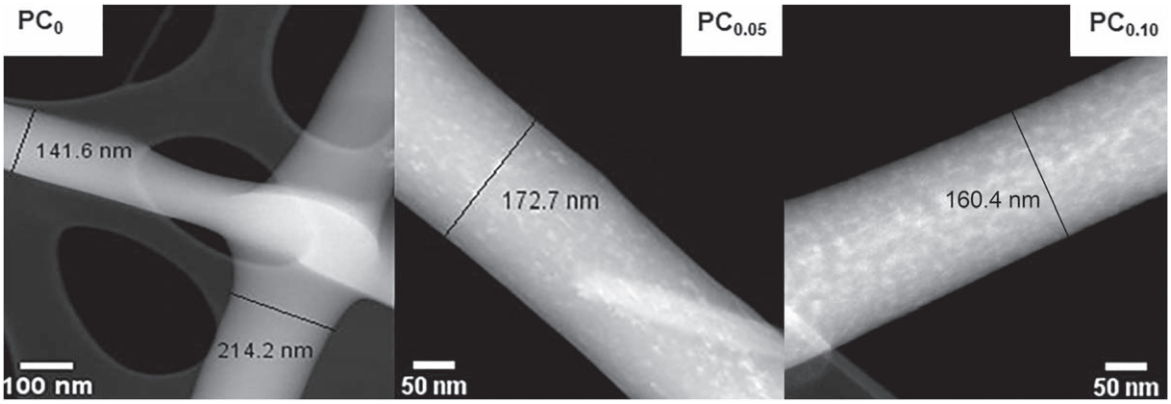

Figure 4. HAADF-STEM images corresponding to the PC_0, $PC_{0.05}$ and $PC_{0.10}$ fibres on the Cu mesh. The non-uniform white contrast in the $PC_{0.05}$ and $PC_{0.10}$ unlike in PC_0 corresponds to the embedded CrI_3 nanoparticles inside the fibres.

CrI_3 increases, as compared to the pure PEO. For $PC_{0.05}$ the evaluated $\langle d \rangle$ and σ are, respectively, 420 and 800 nm, while they were 601 and 1000 nm without CrI_3. Different factors can affect the morphology of these types of systems and, in particular, their diameter. The most important ones are solution concentration and viscosity, electrostatic forces, drying rate and needle diameter. In the present work, adding CrI_3 particles reduces the drying rate (in $PC_{0.05}$), so that the fibres are stretched over a longer period and this results in thinner fibres distributed in the sample [47].

Since CrI_3 is not soluble in the used solvent 2-Propanol, increasing two times the CrI_3 amount (as in $PC_{0.10}$) further affects the solution drying during the electrospinning process and, consequently, further reduces the diameters of the fibres. So, the $PC_{0.10}$ sample is mainly made of a network of very thin fibres with uniform diameters ($\langle d \rangle = 294$ nm, $\sigma = 770$ nm), although some long-thicker fibres are also seen.

STEM analysis in the HAADF mode was done to access the microstructure of the system, and the results are presented in figure 4. For this characterization, a small number of the fibres were gathered on a Cu grid. Whereas the fibres in PC_0 look uniform and smooth, the non-uniformity in the contrast inside the $PC_{0.05}$ and $PC_{0.10}$ fibres mats can be referred to the embedded CrI_3 nanoparticles. According to figure 4, most of the observed nanoparticle inclusions in the PC_x nano/microfibres are in the range 40–50 nm, which is consistent with the grain sizes previously determined from XRD.

3.3. Elemental analysis

The energy dispersion X-ray spectra (EDX) obtained on the fibre samples are depicted in figure 5. The corresponding weight percentages are summarized in table 1. As expected, the EDX spectra present C and O in all samples arising from the PEO polymer matrix. Additionally, peaks corresponding to Cr and I are observed in $PC_{0.05}$ and $PC_{0.10}$.

Some trace elements of Si and Ca are also observed that are already in the pure PEO fibres (PC_0) and are attributed to residual elements in the polymer. For this reason, they were not included in table 1.

Because of the inhomogeneous nature of the samples, with CrI_3 particles dispersed in the polymer fibre matrix, the EDX analysis was performed in different regions. The results of these analyses are depicted as the weight percentage of the present elements along with the ratio of the weight percentage of Iodine to Chromium (I/Cr). This ratio, which is expected to be at about 7.3 Wt% for CrI_3, is identified by *r*. The I/Cr ratio obtained in the fibre mats were 7.13 Wt% for the $PC_{0.05}$

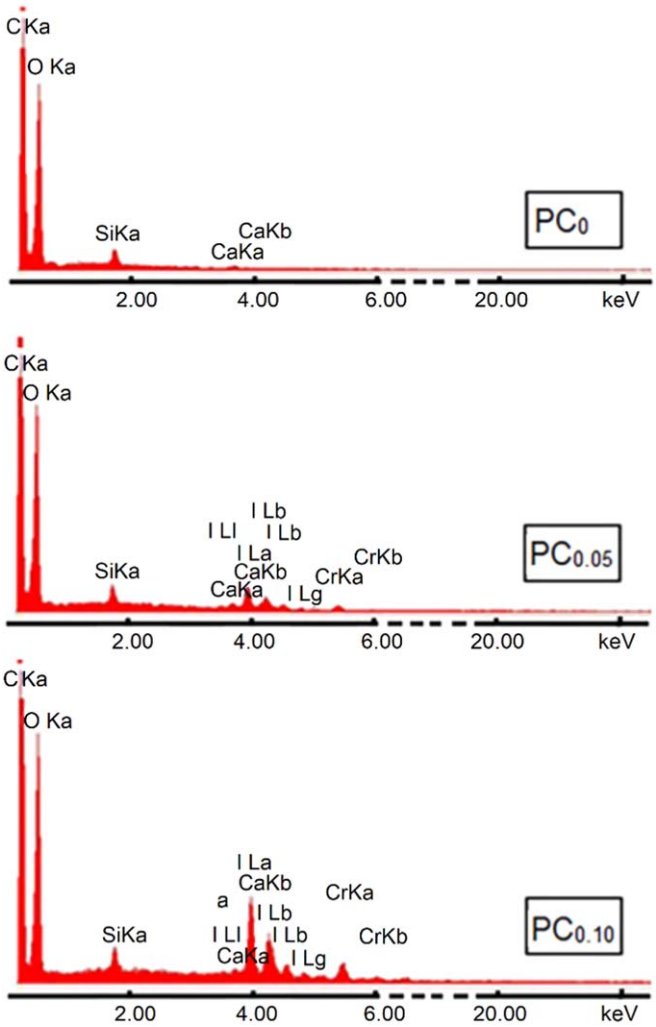

Figure 5. EDX analysis for PC_0, $PC_{0.05}$ and $PC_{0.10}$.

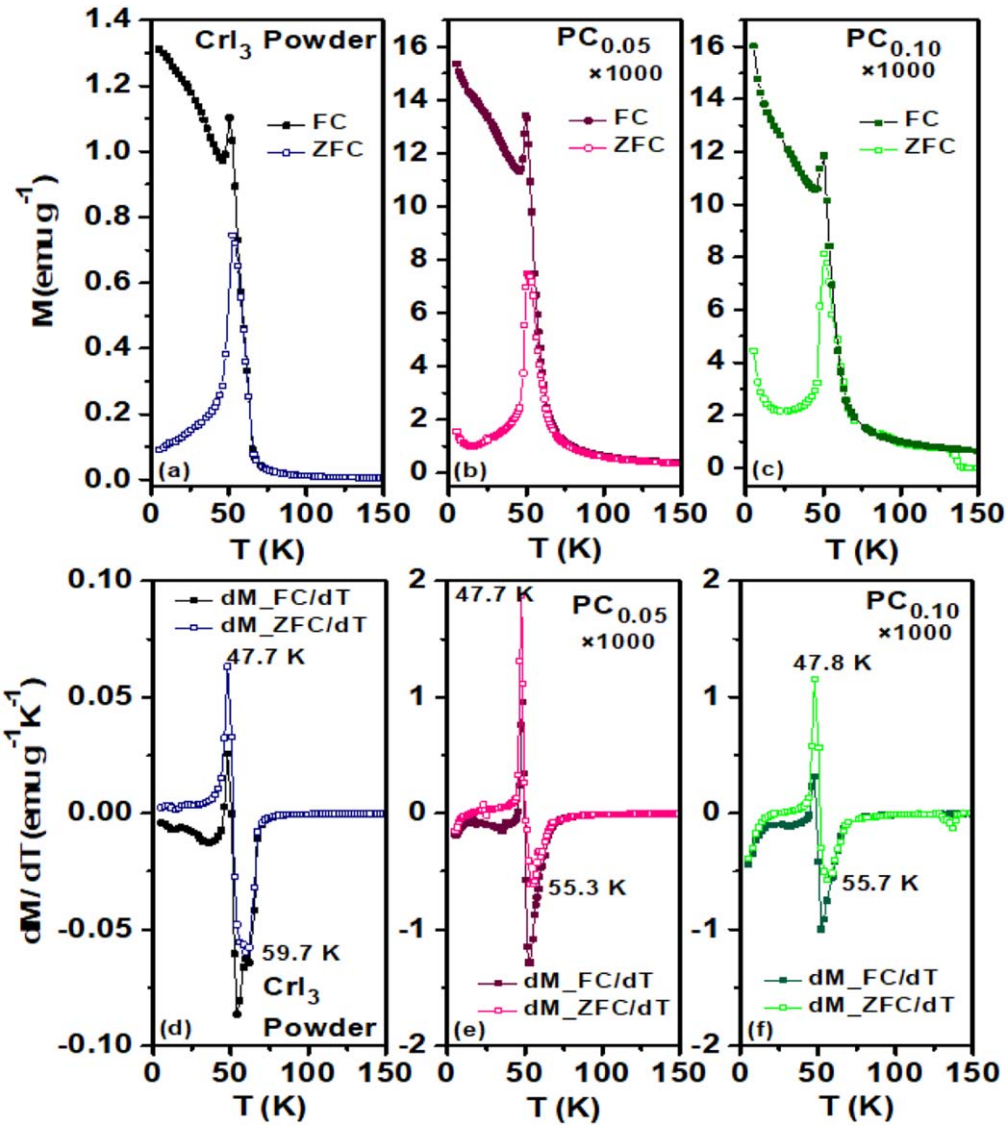

Figure 6. (a)–(c) ZFC (open) and FC (filled symbols) magnetization curves, (d)–(f) dM/dT curves measured under an applied field of 100 Oe for $PC_{0.05}$ and $PC_{0.10}$ in comparison with CrI_3 powder.

Table 1. The weight percentage of the elements corresponding to the EDX spectra obtained for representative areas of the PC_x nano/microfibre samples of figure 3.

	Element [Wt%]				
Sample	C	O	Cr	I	I/Cr
PC_0	62.48	36.46	—	—	—
$PC_{0.05}$	58.25	35.09	0.70	4.98	7.13
$PC_{0.10}$	54.07	31.50	1.50	11.83	7.94

sample and 7.94 Wt% for the $PC_{0.10}$ sample, in complete agreement with the CrI_3 ratio within the error margin of the measurement.

3.4. Magnetic characterization

The temperature dependence of the magnetization was analysed for the PC_x ($x = 0.05$ and 0.10) samples in ZFC and FC procedures. In the former case, the sample was cooled in the absence of a magnetic field while in the FC mode the sample was cooled with an applied magnetic field of 100 Oe. The magnetization measurements were performed during heating, with a 100 Oe applied magnetic field in fibre mat plane. A comparison is also made with the corresponding results on the CrI_3 powder. The results of these studies are presented in figures 6(a)–(c).

A clear paramagnetic (PM) to ferromagnetic (FM) transition is observed in the bulk powder, at ∼61 K, near to the bulk Curie (T_c) temperature previously obtained for this material [21–23]. A similar PM → FM transition is observed in the fibres, at lower temperatures than in the powder.

Determining the dM/dT versus temperature plot extrema is a way to distinguish the transition temperatures of the samples. This study was done, by using both ZFC and FC data for the PC_x samples and the CrI_3 powder (figures 6(d)–(f)). The Curie temperature of the samples can be determined from the minima of the dM/dT curve. It is ∼60 K for the used CrI_3 powder and

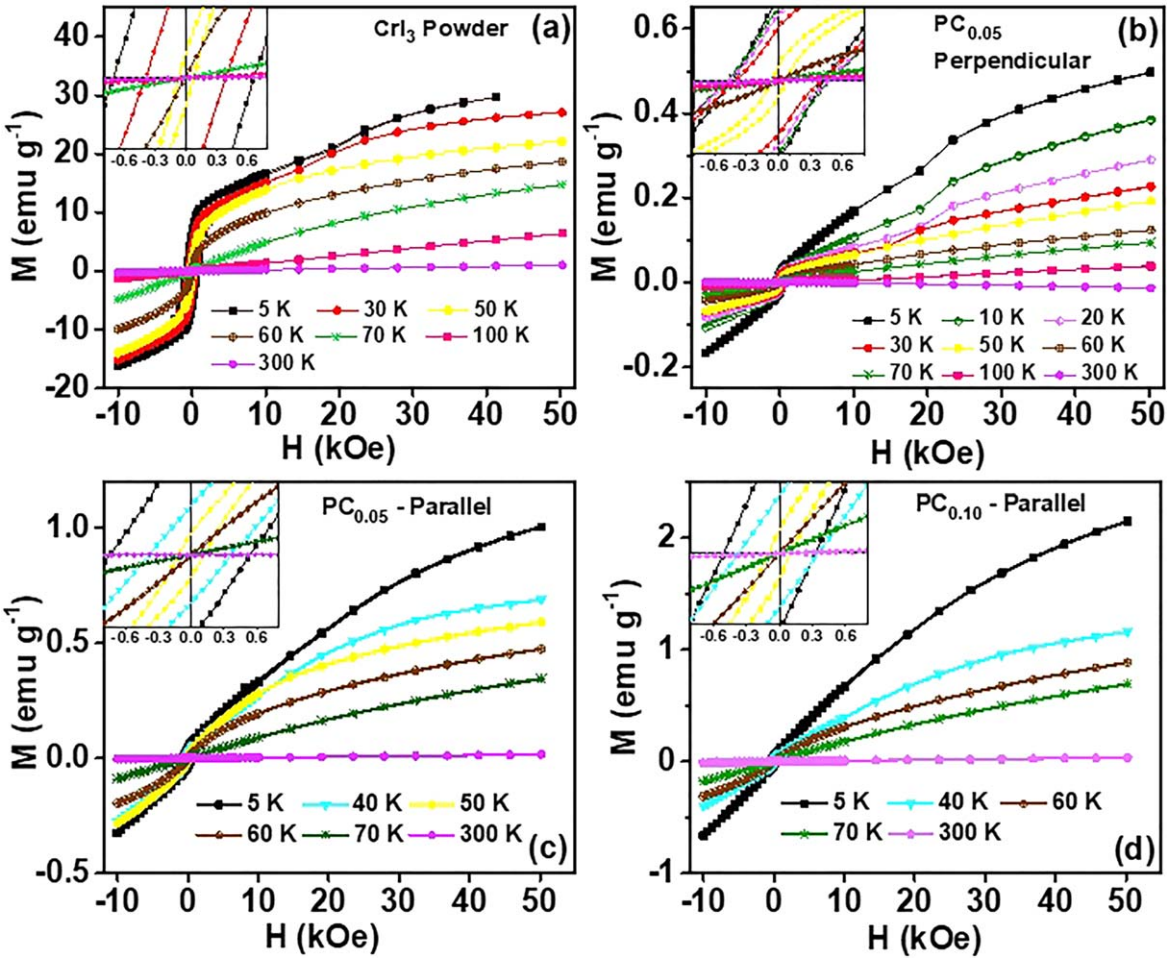

Figure 7. Isothermal magnetization hysteresis cycles for (a) CrI_3 powder, $PC_{0.05}$ under (b) perpendicular and (c) parallel (in-plane) magnetic field and (d) $PC_{0.10}$ under parallel magnetic field. The zoom-in on the low-field M(H) curves region are presented as inset.

lower, ~55–56 K, in the nano/microfibres. This T_c decrease has also been observed in studies of thickness dependent CrI_3 crystals [22], where the reduction of thickness leads to a decrease in T_c. Additionally, previous theoretical studies have determined that the presence of compressive strain tends to decrease the Curie temperature [48]. Here, then, the slight shift in the transition temperatures of the PC_x samples can also be ascribed to the presence of strain on the CrI_3 inclusions, as observed from the XRD results, due to their mechanical interaction with the PEO matrix of the fibres.

In the nano/microfibres the FM → PM transition is somewhat less abrupt than in the powder, as observed by a slower temperature dependent decrease of the magnetization, for T above ~60 K. It is known that the Curie temperature of nanoparticles changes depending on their size [49, 50]. As such, since the CrI_3 inclusions in the nano/microfibres present a size distribution, as observed from the STEM measurements (figure 4), a corresponding T_c distribution arises where some of the particles transition to the paramagnetic phase while others still remain in the ferromagnetic state. This then leads to a distribution of Curie temperatures that manifests as a slower decrease of the magnetization versus temperature profile, as T increases.

From figures 6(d)–(f), it is observed that there is an obvious maximum at T^* ~48 K in all dM/dT versus temperature curves, both for the CrI_3 powder and for the PC_x samples. Similar peaks in the range of 45–48 K have been previously reported by Yu Liu *et al* [22, 24] who termed them as satellite transitions. A crossover from depinning to pinning of magnetic domain walls, as the temperature decreases, has been suggested for the origin of this transition [22]. This would predict that the transition would be less observed in the FC curve, since the domains are already pinned by the effective FM moment alignment along the cooling field [22]. However, this is not observed in our samples, where T^* is similarly observed both in the ZFC and FC curves. According to the literature [22, 51], T^* depends on the external applied magnetic field during the FC and ZFC analysis. Intriguingly, T^* is observed just below the Curie temperature and it is near the value of 45 K identical to the Curie temperature in CrI_3 monolayers measured by magneto-optical Kerr microscopy under $H = 1.5$ kOe [22, 28].

Isothermal magnetization hysteresis cycles were measured for the CrI_3 powder, in the different temperatures from 5 to 300 K, and between −10 and +50.2 kOe. These results are presented in figure 7(a). It is seen that the magnetization of CrI_3 does not saturate up to 40 kOe even at 5 K. Nevertheless, selecting the highest magnetization value (29.7 emu g^{-1}) and using equation (3) to calculate magnetic moment per formula unit in Bohr magnetons, gives 2.3 μ_B. Since the sample

magnetization is not fully saturated, it is somewhat below the theoretical value assuming $g_S = 3\,\mu_B$ and the $3.1\,\mu_B$ determined experimentally by McGuire *et al* [20]. Other reported saturation moments range from 2.7 to 3.0 μ_B/Cr [52, 53]. This difference can be attributed to the isolated magnetic ion clusters that might be present and which do not fully contribute to the overall magnetization. This is in agreement with the observed incomplete saturation of the samples.

$$\mu_{\text{f.u.}}(\mu_B) = \frac{M(\text{emu g}^{-1}) * \text{mol} - W(\text{g})}{9.274 * 10^{-24} * 6.022 * 10^{23}} * 10^{-3}. \qquad (3)$$

Another important point is the presence of the field-driven metamagnetic transition which is seen around 19 kOe at 5 K in the powder and shifts to lower fields by increasing the temperature. The metamagnetic transition was also reported previously for CrI_3 single crystals with thicknesses below 2 micrometres, at about 20 kOe [22, 51].

Similar to the powder, an $M(H)$ study was done for the $PC_{0.05}$ sample, with the applied magnetic field (H) direction both perpendicular and in the plane of the fibre mat samples, and for $PC_{0.10}$ under an in plane magnetic field. These analyses have been presented in the figures 7(b)–(d), respectively. The hysteresis cycles measurements were done between −10 and +50.2 kOe and at different temperatures (from 5 to 300 K). The previous XRD results have shown that the CrI_3 inclusions c-axis is perpendicular to the plane of the nano/microfibre mats and their hexagonal ab planes are in the plane, along the fibres axis. Thus, here, when the applied magnetic field is perpendicular (parallel) to the fibre mat plane, then $H \perp ab$ ($H||ab$) of the CrI_3 inclusions. According to the collected data, an obvious field-driven metamagnetic transition is seen when the field is applied perpendicular to the fibre mat plane ($H \perp ab$), which is more pronounced than the one observed in the powder. At 5 K, the calculated value of the $\delta = (\Delta M/M)$ jump is 14.5% for the CrI_3 powder and 27.4% for $PC_{0.05}$ nano/microfibres under a perpendicular field. Moreover, in the H applied parallel to the mats plane case (figures 7(c), (d)) only a slight change of slope in the M (H) curves is observed.

This indicates that the observed metamagnetic transition is linked to the orientation of the applied field, relative to the layer ab planes of the CrI_3 inclusions in the fabricated fibres. This observation in the CrI_3 powder can be ascribed to its polycrystalline nature, where some of the CrI_3 flakes are still oriented with H perpendicular to ab plane. Similarly, the slight change of $M(H)$ slope in the nano/microfibres, with H applied parallel to the plane of the mats can be ascribed to the remaining slight polycrystallinity, as observed from the XRD results. Figures 8(a), (b) exhibits this phenomenon for CrI_3 powder and $PC_{0.05}$. The detailed analyses for $PC_{0.05}$ under perpendicular direction depicts that the metamagnetic transition field (H^*) also occurs around 19 kOe in the fibres, at 5 K, and changes to lower fields with increasing temperature. The variation of the metamagnetic critical fields (H^*) versus temperature is presented in figure 8(c). This transition disappears above 45 K, for low applied fields, consistent with the $T^* \sim 48$ K determined from the temperature dependent magnetization results of figure 6.

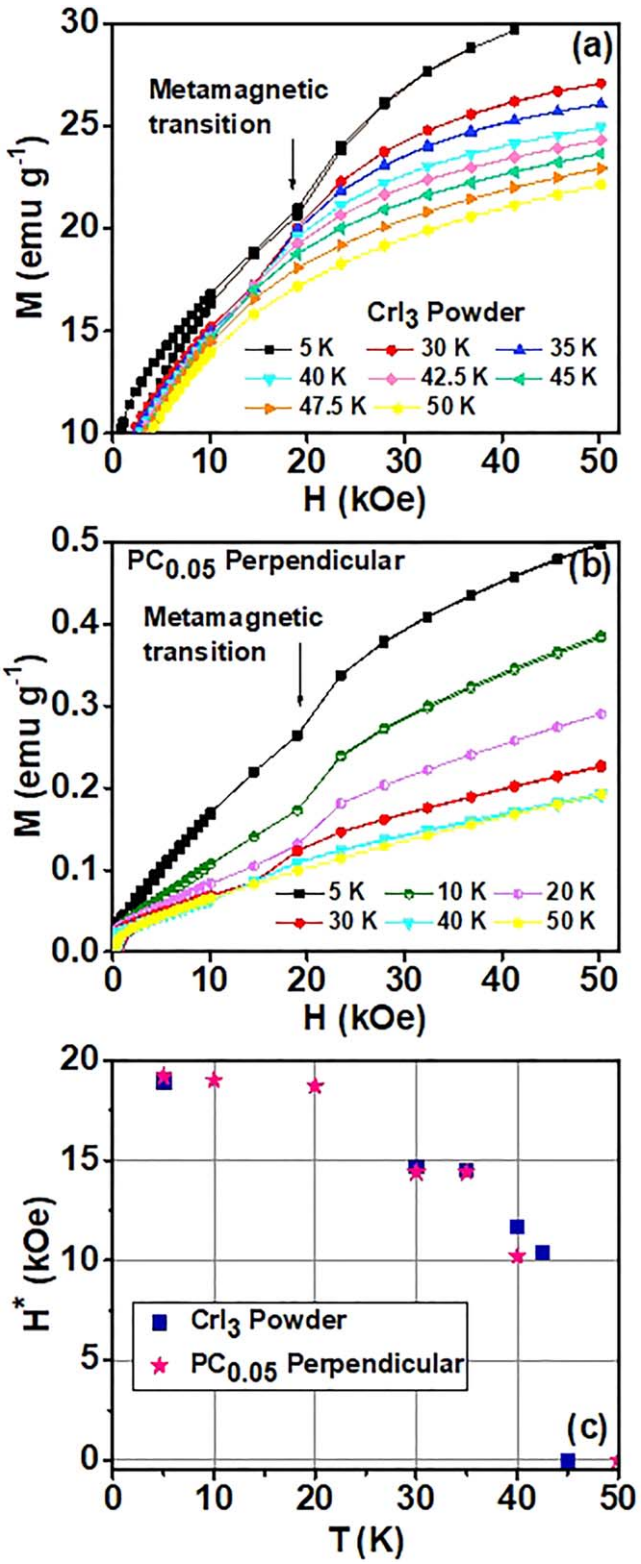

Figure 8. Field-driven metamagnetic transition for (a) CrI_3 powder and (b) $PC_{0.05}$ (under perpendicular magnetic field), (c) variation of the metamagnetic critical field (H^*) versus temperature for CrI_3 powder and $PC_{0.05}$ under perpendicular magnetic field.

Studies have shown that, in thin CrI_3 crystals, the CrI_3 layers order ferromagnetically intralayer, in the ab plane, but may develop interlayer antiferromagnetic ordering, as observed, in particular, in CrI_3 bilayers [27, 28]. Here, when a magnetic

field is applied perpendicular to the fibre mat plane, it is also applied perpendicular to the CrI_3 inclusions *ab* plane, due to their strong orientation inside the nano/microfibres. Then as the magnetic field increases, the layers are forced to be oriented from AFM to FM giving the observed metamagnetic transition. This effect is smaller when the applied fields are in the fibre mat plane, and thus, parallel to the CrI_3 *ab* layers. In this case, the interlayer antiparallel spins rotate continuously and no transition is observed. This effect has been the subject of recent studies, using magnetoresistance data [51, 54].

It has been observed that the metamagnetic transition leads to a high magnetoresistance effect, which is useful in spintronic device designing [51]. Here, the highly oriented CrI_3 inclusions in the electrospun nano/microfibres allows taking advantage of these anisotropic magnetic effects, in these 2D magnetic materials, in a simple and cost effective way.

In addition, studying the isothermal magnetization hysteresis cycles of the PC_x samples, a noticeable coercivity (H_c) in the nano/microfibres is observed below 60 K, as shown in the insets of figures 7(b)–(d) and supplementary material figure S2. This confirms the magnetic ordering behaviour of the fibre mats below 60 K and is consistent with our previous discussion, where the Curie temperature of the samples was estimated to be in 55–56 K, and is also in agreement with the literature [23]. Here, the coercive fields at 5 K are 640 Oe and 415 Oe for $PC_{0.05}$ and $PC_{0.10}$, respectively (inset of figures 7(c), (d) and S2), which are higher than what was previously reported [20, 21, 23] in bulk samples. The values which were reported in [23], for CrI_3 crystals, are about 72 and 85 Oe, when the external magnetic field is parallel and perpendicular to the *c* axis respectively, at 2 K. On the other hand, high coercive fields, of around 920 Oe, have been observed in 50 nm thick samples [22]. This value is near the ones obtained in our CrI_3 fibres, which further confirms the nanoscopic size of the CrI_3 inclusions in our samples. According to the collected data (figure S2) increasing the temperature leads to a decreasing H_c up to the Curie temperature, where the hysteresis disappears and the $M(H)$ loops change to a linear response, characteristic of the paramagnetic behaviour in this temperature range. The minor asymmetry of the hysteresis loops below 60 K, also indicates the presence of an exchange field (H_x) inside the nano/microfibres (figure S2).

In the samples, the H_c values of the fibre mats typically have higher values for $PC_{0.05}$ (figures 7(c), (d)), while $PC_{0.10}$ generally has higher magnetization. This is due to more CrI_3 magnetic material inclusions in $PC_{0.10}$ leading to closer dispersed grains and higher inter particle exchange interactions, opening extra degrees of freedom to tailor the functionalized nano/microfibres magnetic properties.

4. Conclusion

Functionalized magnetic van der Waals CrI_3 nano/microfibres were produced by the electrospinning technique. The nano/microfibres were composed by uniformly dispersed chromium triiodide inclusions, inside the PEO polymer matrix, with sizes of 40–50 nm. They were shown to present the CrI_3 $C2/m$ monoclinic structure, at room temperature, with strong orientation, where the monoclinic *c*-axis was oriented perpendicular to the fibre mat plane. Their magnetic properties presented a FM–PM phase transition, with a lower transition temperature as compared with bulk samples. Additionally, a strong field-induced metamagnetic transition was observed when the magnetic field was applied perpendicular to the fibre's plane, that disappeared above 45 K. The transition was hindered when the magnetic field was in the fibre mat plane. This metamagnetic transition was determined to be due to the crossover from AFM to FM interlayer magnetic moments orientation, along the CrI_3 *c*-axis, induced by the perpendicular applied magnetic field. These well-oriented van der Waals CrI_3 inclusions inside electrospun nano/microfibres then show a good cost-effective way to develop magnetic functionalized fibres for spintronic applications, taking advantage of the 2D layered anisotropic materials properties.

Acknowledgments

We are grateful to the Fundação Para a Ciência e a Tecnologia (FCT) for the financial support through the Physics Centers of the Universities of Minho and Porto (Ref. UIDB/04650/2020) and projects UTAPEXPL/NTec/0046/2017, NORTE-01-0145-FEDER-028538 and PTDC/FIS-MAC/29454/2017. J H Belo thanks FCT for the Grant SFRH/BD/88440/2012, the project PTDC/FIS-MAC/31302/2017 and his contract DL57/2016 reference SFRH-BPD-87430/2012. J P Araújo and J H Belo thank the funding from the project, with reference POCI-01-0145-FEDER- 032527. V B Isfahani acknowledges a Post-Doc grant from the project NORTE-01-0145-FEDER-028538. L Boddapati acknowledges the Nano TRAIN for Growth II program by the European Commission through the Horizon 2020 Marie Sklodowska-Curie COFUND Programme and support provided by the International Iberian Nanotechnology Laboratory. We are gratefull to Professor Michael Belsley, of the Physics Department at Minho University, for the fruitfull discussions on the manuscript.

ORCID iDs

Vahideh Bayzi Isfahani https://orcid.org/0000-0003-4321-217X
Rosa Maria Ferreira Baptista https://orcid.org/0000-0002-5380-9212
Etelvina de Matos Gomes https://orcid.org/0000-0002-0862-1683

References

[1] Novoselov K-S, Geim A-K, Morozov S-V, Jiang D, Zhang Y, Dubonos S-V, Grigorieva I-V and Firsov A-A 2004 Electric field effect in atomically thin carbon films *Science* **306** 666–9

[2] Choi W, Choudhary N, Han G-H, Park J, Akinwande D and Lee Y-H 2017 Recent development of two-dimensional transition metal dichalcogenides and their applications *Mater. Today* **20** 116–30

[3] Yao J, Zheng Z and Yang G 2019 Production of large-area 2D materials for high-performance photodetectors by pulsed-laser deposition *Prog. Mater Sci.* **106** 100573

[4] Lee W-H and Park Y-D 2018 Tuning electrical properties of 2D materials by self-assembled monolayers *Adv. Mater. Interfaces* **5** 1700316

[5] Akinwande D, Brennan C-J, Bunch J-S, Egberts P, Felts J-R, Gao H, Huang R, Kim J-S, Li T and Li Y 2017 A review on mechanics and mechanical properties of 2D materials-graphene and beyond *Extreme Mech. Lett.* **13** 42–77

[6] Li X, Sun M, Shan C, Chen Q and Wei X 2018 Mechanical properties of 2D materials studied by *in situ* microscopy techniques *Adv. Mater. Interfaces* **5** 1701246

[7] Mannix A-J, Kiraly B, Hersam M-C and Guisinger N-P 2017 Synthesis and chemistry of elemental 2D materials *Nat. Rev. Chem.* **1** 1–14

[8] Jansen R, Dash S-P, Sharma S and Min B 2012 Silicon spintronics with ferromagnetic tunnel devices *Semicond. Sci. Technol.* **27** 083001

[9] Chen W, George J, Varley J-B, Rignanese G-M and Hautier G 2019 High-throughput computational discovery of $In_2Mn_2O_7$ as a high Curie temperature ferromagnetic semiconductor for spintronics *npj Comput. Mater.* **5** 72

[10] Cheng F, Du Z, Wang X, Cai Z, Li L, Wang C, Benabbas A, Champion P, Sun N and Pan L 2020 All-optical helicity-dependent switching in hybrid metal-ferromagnet thin films *Adv. Opt. Mater.* **8** 2000379

[11] Hankiewicz J, Celinski Z, Stupic K, Anderson N and Camley R 2016 Ferromagnetic particles as magnetic resonance imaging temperature sensors *Nat. Commun.* **7** 1–8

[12] Morón C, Cabrera C, Morón A, García A and González M 2015 Magnetic sensors based on amorphous ferromagnetic materials: a review *Sensors* **15** 28340–66

[13] Liu M, Howe B-M, Grazulis L, Mahalingam K, Nan T, Sun N-X and Brown G-J 2013 Voltage-impulse-induced non-volatile ferroelastic switching of ferromagnetic resonance for reconfigurable magnetoelectric microwave devices *Adv. Mater.* **25** 4886–92

[14] Fina I, Dix N, Rebled J, Gemeiner P, Marti X, Peiro F, Dkhil B, Sanchez F, Fabrega L and Fontcuberta J 2013 The direct magnetoelectric effect in ferroelectric-ferromagnetic epitaxial heterostructures *Nanoscale* **5** 8037–44

[15] Ikenaga M, Ohura K, Yamamuro T, Kotoura Y, Oka M and Kokubo T 1993 Localized hyperthermic treatment of experimental bone tumors with ferromagnetic ceramics *J. Orthop. Res.* **11** 849–55

[16] Mitxelena-Iribarren O, Campisi J, de Apellániz I-M, Lizarbe-Sancha S, Arana S, Zhukova V, Mujika M and Zhukov A 2020 Glass-coated ferromagnetic microwire-induced magnetic hyperthermia for *in vitro* cancer cell treatment *Mater. Sci. Eng.* C **106** 110261

[17] Saito H, Mitobe K, Ito A, Sugawara Y, Maruyama K, Minamiya Y, Motoyama S, Yoshimura N and Ogawa J-I 2008 Self-regulating hyperthermia induced using thermosensitive ferromagnetic material with a low Curie temperature *Cancer Sci.* **99** 805–9

[18] Liu W and Xu Y (ed) 2020 *Spintronic 2D Materials: Fundamentals and Applications* (Amsterdam: Elsevier)

[19] McGuire M-A 2019 Crystal and magnetic structures in layered, transition metal dihalides and trihalides *Crystals* **7** 121

[20] McGuire M-A, Dixit H, Cooper V-R and Sales B-C 2015 Coupling of crystal structure and magnetism in the layered, ferromagnetic insulator CrI_3 *Chem. Mater.* **27** 612–20

[21] Liu Y and Petrovic C 2018 Three-dimensional magnetic critical behavior in CrI_3 *Phys. Rev.* B **97** 014420

[22] Liu Y, Wu L, Tong X, Li J, Tao J, Zhu Y and Petrovic C 2019 Thickness-dependent magnetic order in CrI_3 single crystals *Sci. Rep.* **9** 1–8

[23] Mondal S, Kannan M, Das M, Govindaraj L, Singha R, Satpati B, Arumugam S and Mandal P 2019 Effect of hydrostatic pressure on ferromagnetism in two-dimensional CrI_3 *Phys. Rev.* B **99** 180407

[24] Liu Y and Petrovic C 2018 Anisotropic magnetocaloric effect in single crystals of CrI_3 *Phys. Rev.* B **97** 174418

[25] Jiang P, Wang C, Chen D, Zhong Z, Yuan Z, Lu Z-Y and Ji W 2019 Stacking tunable interlayer magnetism in bilayer CrI_3 *Phys. Rev.* B **99** 144401

[26] Sivadas N, Okamoto S, Xu X, Fennie C-J and Xiao D 2018 Stacking-dependent magnetism in bilayer CrI_3 *Nano Lett.* **18** 7658–64

[27] Seyler K-L, Zhong D, Klein D-R, Gao S, Zhang X, Huang B, Navarro-Moratalla E, Yang L, Cobden D-H and McGuire M-A 2018 Ligand-field helical luminescence in a 2D ferromagnetic insulator *Nat. Phys.* **14** 277–81

[28] Huang B, Clark G, Navarro-Moratalla E, Klein D-R, Cheng R, Seyler K-L, Zhong D, Schmidgall E, McGuire M-A and Cobden D-H 2017 Layer-dependent ferromagnetism in a van der Waals crystal down to the monolayer limit *Nature* **546** 270–3

[29] Anderson P-W 1950 Antiferromagnetism. Theory of superexchange interaction *Phys. Rev.* **79** 350

[30] Xu R and Zou X 2020 Electric field-modulated magnetic phase transition in van der Waals CrI_3 bilayers *J. Phys. Chem. Lett.* **11** 3152–8

[31] Shcherbakov D, Stepanov P, Weber D, Wang Y, Hu J, Zhu Y, Watanabe K, Taniguchi T, Mao Z and Windl W 2018 Raman spectroscopy, photocatalytic degradation, and stabilization of atomically thin chromium tri-iodide *Nano Lett.* **18** 4214–9

[32] Niu B, Su T, Francisco B-A, Ghosh S, Kargar F, Huang X, Lohmann M, Li J, Xu Y and Taniguchi T 2019 Coexistence of magnetic orders in two-dimensional magnet CrI_3 *Nano Lett.* **20** 553–8

[33] Agarwal S, Wendorff J-H and Greiner A 2008 Use of electrospinning technique for biomedical applications *Polymer* **49** 5603–21

[34] Mali S-S, Patil P-S and Hong C-K 2014 Low-cost electrospun highly crystalline kesterite Cu_2ZnSnS_4 nanofiber counter electrodes for efficient dye-sensitized solar cells *ACS Appl. Mater. Interfaces* **6** 1688–96

[35] Döpke C, Grothe T, Steblinski P, Klöcker M, Sabantina L, Kosmalska D, Blachowicz T and Ehrmann A 2019 Magnetic nanofiber mats for data storage and transfer *Nanomaterials.* **9** 92

[36] Huang W, Tong Z, Wang R, Liao Z, Bi Y, Chen Y, Ma M, Lyu P and Ma Y 2020 A review on electrospinning nanofibers in the field of microwave absorption *Ceram. Int.* **46** 26441–53

[37] Chen X, Ge X, Qian Y, Tang H, Song J, Qu X, Yue B and Yuan W-E 2020 Electrospinning multilayered scaffolds loaded with melatonin and Fe_3O_4 magnetic nanoparticles for peripheral nerve regeneration *Adv. Funct. Mater.* **30** 2004537

[38] Babincová N, Jirsák O, Babincová M, Babinec P and Šimaljaková M 2020 Remote magnetically controlled drug release from electrospun composite nanofibers: design of a smart platform for therapy of psoriasis *Z. Naturforsch.* A **75** 587–91

[39] Xue J, Wu T, Dai Y and Xia Y 2019 Electrospinning and electrospun nanofibers: methods, materials, and applications *Chem. Rev.* **119** 5298–415

[40] Sá P, Barbosa J, Bdikin I, Almeida B, Rolo A-G, de Matos Gomes E, Belsley M, Kholkin A-L and Isakov D 2013 Ferroelectric characterization of aligned barium titanate nanofibres *J. Phys. D: Appl. Phys.* **46** 105304

[41] Isakov D-V, de Matos Gomes E, Vieira L-G, Dekola T, Belsley M-S and Almeida B-G 2011 Oriented single-crystal-like molecular arrangement of optically nonlinear 2-methyl-4-nitroaniline in electrospun nanofibers *ACS Nano* **5** 73–8
[42] Isakov D, de Matos Gomes E, Almeida B, Bdikin I, Martins A and Kholkin A 2010 Piezoresponse force microscopy studies of the triglycine sulfate-based nanofibers *J. Appl. Phys.* **108** 042011
[43] Isakov D, de Matos Gomes E, Belsley M, Almeida B, Martins A, Neves N and Reis R 2010 High nonlinear optical anisotropy of urea nanofibers *Europhys. Lett.* **91** 28007
[44] Kakade M-V, Givens S, Gardner K, Lee K-H, Chase D-B and Rabolt J-F 2007 Electric field induced orientation of polymer chains in macroscopically aligned electrospun polymer nanofibers *J. Am. Chem. Soc.* **129** 2777–82
[45] Dror Y, Salalha W, Khalfin R-L, Cohen Y, Yarin A-L and Zussman E 2003 Carbon nanotubes embedded in oriented polymer nanofibers by electrospinning *Langmuir* **19** 7012–20
[46] Matsumoto H, Imaizumi S, Konosu Y, Ashizawa M, Minagawa M, Tanioka A, Lu W and Tour J-M 2013 Electrospun composite nanofiber yarns containing oriented graphene nanoribbons *ACS Appl. Mater. Interfaces* **5** 6225–31
[47] Sun B, Long Y, Zhang H, Li M, Duvail J, Jiang X and Yin H 2014 Advances in three-dimensional nanofibrous macrostructures via electrospinning *Prog. Polym. Sci.* **39** 862–90
[48] Liu J, Sun Q, Kawaze Y and Jena P 2016 Exfoliating biocompatible ferromagnetic Cr-trihalide monolayers *PCCP* **18** 8777–84
[49] Cao L-F, Dan X, Guo M-X, Park H and Fujita T 2007 Size and shape effects on Curie temperature of ferromagnetic nanoparticles *Trans. Nonferrous Met. Soc. China* **17** 1451–5
[50] Chhabra H and Kumar M 2019 Modeling for size and shape dependence of critical temperature for different type of nanomaterials *J. Phys. Chem. Solids* **135** 109075
[51] Kim H-H, Yang B, Patel T, Sfigakis F, Li C, Tian S, Lei H and Tsen A-W 2018 One million percent tunnel magnetoresistance in a magnetic van der Waals heterostructure *Nano Lett.* **18** 4885–90
[52] Carteaux V, Brunet D, Ouvrard G and Andre G 1995 Crystallographic, magnetic and electronic structures of a new layered ferromagnetic compound $Cr_2Ge_2Te_6$ *J. Phys.: Condens. Matter* **7** 69
[53] Ji H, Stokes R, Alegria L, Blomberg E, Tanatar M, Reijnders A, Schoop L, Liang T, Prozorov R and Burch K 2013 A ferromagnetic insulating substrate for, the epitaxial growth of topological insulators *J. Appl. Phys.* **114** 114907
[54] Klein D-R, MacNeill D, Lado J-L, Soriano D, Navarro-Moratalla E, Watanabe K, Taniguchi T, Manni S, Canfield P and Fernández-Rossier J 2018 Probing magnetism in 2D van der Waals crystalline insulators via electron tunneling *Science* **360** 1218–22